Available online at www.sciencedirect.com
SCIENCE DIRECT®
Journal of Solid State Chemistry 177 (2004) 4428–4442
JOURNAL OF SOLID STATE CHEMISTRY
www.elsevier.com/locate/jssc

A structure, conductivity and dielectric properties investigation of $A_3CoNb_2O_9$ ($A = Ca^{2+}$, Sr^{2+}, Ba^{2+}) triple perovskites

V. Ting[a], Y. Liu[a], L. Norén[a], R.L. Withers[a,*], D.J. Goossens[a], M. James[b], C. Ferraris[c]

[a] *Research School of Chemistry, The Australian National University, Solid State Structural Chemistry, Canberra, ACT 0200, Australia*
[b] *Bragg Institute, Australian Nuclear Science and Technology Organisation, PMB 1, Menai NSW 2234, Australia*
[c] *Institute of Environmental Science and Engineering, Nanyang Technological University (NTU), Innovation Centre Block 2, Unit 247, 18 Nanyang Drive, Singapore 637723, Singapore*

Received 18 June 2004; received in revised form 31 August 2004; accepted 9 September 2004

Abstract

The room temperature structures as well as the temperature-dependent conductivity and dielectric properties of the $A_3CoNb_2O_9$ ($A = Ca^{2+}$, Sr^{2+} and Ba^{2+}) triple perovskites have been carefully investigated. A constrained modulation wave approach to Rietveld structure refinement is used to determine their room temperature crystal structures. Correlations between these crystal structures and their physical properties are found. All three compounds undergo insulator to semiconductor phase transitions as a function of increasing temperature. The hexagonal $Ba_3CoNb_2O_9$ compound acts as an insulator at room temperature, while the monoclinic $Ca_3CoNb_2O_9$ compound is already a semiconductor at room temperature. The measured dielectric frequency characteristics of the $A = Ba$ compound are excellent.

Keywords: $A_3CoNb_2O_9$ complex perovskites; Dielectric properties; Resistivity insulator to semiconductor phase transitions; Rietveld refinement

1. Introduction

There has recently been renewed interest in the structures [1,2] and associated physical properties of $A_3Co^{2+}Nb_2^{5+}O_9$ ($A = Ca$, Sr and Ba) complex 1:2 perovskites, mainly as a result of their potential photocatalytic [1] and microwave dielectric [3–8] applications. Yin et al. [1] recently reported that these compounds had the ability to act as visible light driven photocatalysts while the $A = Ba$ compound, and appropriately doped variants thereof, are known to have excellent dielectric properties at microwave frequencies [4,6–8]. The relationship between local crystal structure, microstructure and physical properties, however, remains poorly understood for such compounds [6–9]. Why, for example, should the microwave dielectric constant, the Q-value and the temperature coefficient of resonance for $Ba_3CoNb_2O_9$ be distinctly better than those of $Ca_3CoNb_2O_9$? Likewise, why do the band gaps of the $A_3Co^{2+}Nb_2^{5+}O_9$ perovskites extracted from diffuse reflectance spectroscopy show a direct inverse correlation with ionic radius of the A cation whilst the associated visible light photocatalytic properties apparently vary non-systematically with A cation size [1]?

Yin et al. [1] suggested that this latter effect is due to ".. the special (monoclinic rather than ideal cubic) crystal symmetry.." of the Ca compound and presented both model and calculated electronic band structures in support of this interpretation of their observed experimental data. These electronic band structure models and calculations, however, were based upon a reported random distribution of Co^{2+} and Nb^{5+} ions onto the perovskite B-site positions of all these compounds (and hence $Pm\bar{3}m$, $a = a_p$, space group symmetry for the $A = Ba$ and Sr compounds and a monoclinically

*Corresponding author. Fax: +61 2 6125 0750.
E-mail address: withers@rsc.anu.edu.au (R.L. Withers).

0022-4596/$ - see front matter © 2004 Elsevier Inc. All rights reserved.
doi:10.1016/j.jssc.2004.09.016

distorted variant thereof in the case of the $A=Ca$ compound). A recent TEM investigation, however, has found that each of these compounds exhibit clear diffraction evidence for *B*-site ordering and that *none* of them can be described in the space group $Pm\bar{3}m$ [2]. It would appear that Yin et al.'s interpretation of the correlation between "structure" and properties based on the model of a "*B*-site disordered perovskite" (including the model and theoretical band structure calculations) must be seen as uncertain at best.

It is well known, for example, that *B*-site ordering in complex perovskites of this type can have a large effect upon microwave dielectric properties, in particular the dielectric loss properties [3–12] (".. higher (*B* site) ordering correlates with higher *Q*-factor.." [5]). In the particular case of the $A=Ba$ compound, a *B*-site order–disorder phase transition at ~1425 °C has been reported to occur and shown to have a strongly deleterious effect upon the microwave dielectric loss property [6]. The *Q*-value of the *B*-site ordered phase was found to be significantly higher than for the disordered variant [6]. Ahn et al. [7,8] also report a significant decrease in the *Q*-value of the $A=Ba$ compound for sintering temperatures above 1400 °C. This time, however, it is correlated with the onset of CoO evaporation as well as a reduced degree of *B*-site ordering.

Given this background, in conjunction with the absence of detailed information as regards the structures and related dielectric and conductivity properties of these materials, it was decided that a careful investigation into the structure and physical properties of $A_3CoNb_2O_9$ ($A=Ca$, Sr and Ba) complex perovskites was clearly warranted. It is emphasized that the prime purpose of this investigation was to determine the crystal structures and relative physical properties across the members of this compound series rather than to optimize the specific microwave dielectric loss properties of the $A=Ba$ compound.

2. Experimental

2.1. Synthesis

Stoichiometric ratios of $BaCO_3$ (4N, Aldrich), $SrCO_3$ (5 N, Alfa) or $CaCO_3$ (5 N, Alfa) were mixed together with $Co(NO_3)_2\cdot 6H_2O$ (97%, M&B) and Nb_2O_5 (>3 N, Alfa) and ground to a uniform slurry under ethanol in an agate mortar. The resultant mixture was first thermally treated in an 850 °C furnace for a 20 h period to drive off CO_2, then pressed into pellets and calcined at 1230 °C for periods of 48 h with intermediate grinding and re-pelleting.

The calcination temperature used, while somewhat lower than the generally reported firing temperatures (~1400 °C) used for these compounds [4,6] when attempting to optimize the microwave dielectric loss property, has nonetheless been shown to give rise to well-ordered material [1,2] suitable for Rietveld refinement. The use of a lower annealing temperature also minimizes the risk that the stoichiometry of the compound could change due to Co volatilization [7,8]. The bulk densities of the fired $A_3CoNb_2O_9$ ($A=Ba^{2+}$, Sr^{2+} and Ca^{2+}) pellets were determined by the liquid displacement method [13] as 6.25, 5.48 and 4.52 g/cm^3, corresponding to theoretical densities of 96%, 97% and 96%, respectively.

2.2. Powder diffraction

The phase purity and unit cell parameters of the synthesized 1:2 triple perovskite samples were initially investigated by X-ray powder diffraction using a Guinier-Hägg XRD camera with Cu$K\alpha_1$ radiation. Silicon (NBS No. 640c) was added as an internal standard for accurate determination of the unit cell dimensions, which were refined using the "Unitcell" software package [14].

Neutron powder diffraction data for Rietveld refinement were collected at the HIFAR facility at the Australian Nuclear Science and Technology Organisation (ANSTO) using the HRPD instrument at a wavelength of ~1.883 Å. The diffractometer consists of 24 ^{3}He detectors individually separated by 5° and the pattern was collected at room temperature between 5° and 150° in 2θ in steps of 0.05° using a aluminum capped vanadium cylinder as the sample holder.

2.3. Electrical measurements

Silver paste (Dupont) was brushed onto the two surfaces of previously polished pellets of the appropriate compound, which were then subject to a thermal treatment at 500 °C for 30 min for solidification and to ensure good electrical contact as electrodes. Pt wire was then affixed upon the two electrodes for high temperature measurement. The dielectric properties (dielectric constant and dielectric loss) were then measured using a high precision LCR meter (Agilent 4284A) while the resistivity was measured with a multimeter (HP3478A) using the four-probe method. The temperature dependence of the properties was measured up to 500 °C in a temperature-controllable furnace.

2.4. Electron microscopy

High-resolution transmission electron microscope (HRTEM) images were collected using a high contrast objective aperture of 20 mm, corresponding to a nominal point-to-point resolution of 1.9 Å. All the observations were performed at 300 kV on a JEOL

JEM 3010 electron microscope at the CARE-IESE-NTU of Singapore. The microscope was equipped with STEM, Gatan Image Filter (GIF 2000®), LaB_6 cathode, and LINK ISIS EDS X-ray microanalyzer.

3. Results and discussion

3.1. Structure refinements

The X-ray powder patterns of all three compounds appeared single phase. The powder pattern of $Ba_3CoNb_2O_9$ was indexed to a $P\bar{3}m1$ hexagonal cell with unit cell parameters $a=5.7737(4)$ Å and $c=7.0852(9)$ Å. The strontium and calcium compounds were indexed to $P2_1/c$ monoclinic cells, $a=9.7828(7)$ Å, $b=6.6429(5)$ Å, $c=16.980(2)$ Å and $\beta=125.205(7)^\circ$ in the case of $Sr_3CoNb_2O_9$, and $a=9.5985(6)$ Å, $b=5.4685(4)$ Å, $c=16.8094(9)$ Å and $\beta=125.719(4)^\circ$ in the case of $Ca_3CoNb_2O_9$.

The neutron powder diffraction patterns were refined using the Rietveld method [15] and the program packages Rietica [16] and FULLPROF [17]. The following parameters were used. The background was fitted using a polynomial with six refineable parameters. The zero point was refined as well as a scale factor. The variation in peak shape was described with a pseudo-Voigt function with three parameters describing the line width and a further parameter to describe the mixing between Lorentzian and Gaussian contributions. The asymmetry below 40° was corrected for using one further parameter. The other parameters varied were the atomic co-ordinates, the atomic displacement parameters (ADPs) and the unit cell parameters. Given that the observations to parameters ratio is in general not overly high for these compounds, in particular for the $A=$Sr and Ca compounds, the nominally independent ADPs of like ions were usually constrained to refine together in order to avoid over-parameterization.

The lattice parameters were first fixed to those obtained from the X-ray diffraction data and the wavelength refined to give as good a fit as possible to the data (using Rietica [16]). The value for $\lambda_{neutron}$ was then fixed and the unit cell parameters allowed to vary. The obtained wavelengths obtained in this manner were 1.8841(4) Å for $Ba_3CoNb_2O_9$, 1.8835(5) Å for $Sr_3CoNb_2O_9$ and 1.8831(5) Å for $Ca_3CoNb_2O_9$.

3.2. $Ba_3CoNb_2O_9$

3.2.1. Fully B-site ordered refinement

The $P\bar{3}m1$, $\mathbf{a}_h=\mathbf{b}_p-\mathbf{c}_p$, $\mathbf{b}_h=\mathbf{c}_p-\mathbf{a}_p$, $\mathbf{c}_h=\mathbf{a}_p+\mathbf{b}_p+\mathbf{c}_p$ ($\mathbf{a}^*_h=\frac{1}{3}[\bar{1}2\bar{1}]^*_p$, $\mathbf{b}^*_h=\frac{1}{3}[\bar{2}11]^*_p$, $\mathbf{c}^*_h=\frac{1}{3}[111]^*_p$; subscript "p" for perovskite parent sub-structure) supercell of the $Ba_3CoNb_2O_9$ compound contains six independent atom sites, each of which are on special positions. There are only four unknown fractional co-ordinate positions to be refined. They can be written in the form $\frac{1}{6}+\varepsilon_O$, $\frac{1}{3}-\varepsilon'_O$, $\frac{1}{6}+\varepsilon_{Nb}$ and $\frac{1}{6}+\varepsilon_A$ (see e.g. [2] and Table 1). The four displacive parameters, ε_O, ε'_O, ε_{Nb} and ε_A, correspond to the displacive shifts or relaxations away from the parent perovskite positions induced by the Co^{2+}/Nb^{5+} ordering, and are necessarily associated with the same modulation wave-vector describing the Co^{2+}/Nb^{5+} ordering i.e., $\mathbf{q}=\frac{1}{3}[111]^*_p$. The positive parameters ε_O and ε'_O, for example, describe the crystal chemically necessary expansion and contraction in relative size of the CoO_6 and NbO_6 octahedra while the ε_{Nb} parameter describes the also crystal chemically necessary shift of the Nb ion away from the center of its surrounding octahedra of oxygen ions (see [2] for details).

Values for these four unknown parameters (and hence for the unknown fractional co-ordinates) have previously been estimated from a $\mathbf{q}=\frac{1}{3}[111]^*_p$ modulation wave approach based upon crystal chemical/bond valence sum considerations (see [2]). Using $P\bar{3}m1$ space group symmetry and these predicted fractional co-ordinates as starting co-ordinates, the structure of $Ba_3CoNb_2O_9$ was then refined. Given that there are an order of magnitude less fractional co-ordinates to determine for this $A=$Ba compound relative to the $A=$Sr or Ca compounds, the ADPs for the two independent Ba ions, as well as those for the two O ions, were initially refined independently. Since no significant change occurred in either the value of these ADPs or of the refinement statistics when they were allowed to refine separately, like ions were thereafter constrained to refine with the same ADP.

The refinement converged quickly, after which it became clear that some weak additional peaks still remained unaccounted for. These few weak additional peaks were identified as originating from the aluminum in the caps of the sample holder. They did not overlap significantly with the sample peaks, however, and could thus be treated as excluded regions in the refinement. The pattern was also refined with aluminum as a secondary phase. Similar refinement statistics were obtained. The former approach was finally chosen since the aluminum peaks originated from a solid placed at a geometrically different position than that of the sample thus requiring additional parameters to refine properly with no improvement in refinement statistics as a result.

This final refinement (assumed to be fully *B*-site ordered) gave the following statistics for the Rietica/(FULLPROF) refinement respectively (note that R_{Bragg} is defined differently in the two programs cf. [16] and [17]): R_p 4.50/(4.51), R_{wp} 5.53/(5.57), χ^2 2.07/(2.15) and R_{Bragg} 1.21/(3.60) using 23 parameters in total for the 118 theoretical reflections. The Durbin-Watson *d*-statistics parameters (1.14 and 1.90 as given by the FULLPROF refinement), indicated that some

Table 1
Refined structural parameters and resulting AV values obtained from the various refinements of $Ba_3CoNb_2O_9$

Atom	x	y	z	B	AV	Occ
Ba1	0	0	0	0.53(6)	2.473	1.00
	0	0	0	*	2.471	1.00
	0	0	0	*	2.496	0.875(5)
	0	0	0	*	2.375	1.00
Ba2	$\frac{1}{3}$	$\frac{2}{3}$	0.6640(13)	0.53(6)	2.339	1.00
	$\frac{1}{3}$	$\frac{2}{3}$	0.6641(15)	*	2.340	1.00
	$\frac{1}{3}$	$\frac{2}{3}$	0.6635(25)	*	2.326	0.875(5)
	$\frac{1}{3}$	$\frac{2}{3}$	0.6667	*	2.371	1.00
Co	0	0	$\frac{1}{2}$	0.47(25)	1.919	1.00
	0	0	$\frac{1}{2}$	*	1.902	0.91(5)
	0	0	$\frac{1}{2}$	*	1.849	0.875(5)
	0	0	$\frac{1}{2}$	*	1.802	1.00
Nb	$\frac{1}{3}$	$\frac{2}{3}$	0.1762(12)	0.42(8)	4.723	1.00
	$\frac{1}{3}$	$\frac{2}{3}$	0.1762(14)	*	4.748	0.95(5)
	$\frac{1}{3}$	$\frac{2}{3}$	0.1788(21)	*	4.849	0.875(5)
	$\frac{1}{3}$	$\frac{2}{3}$	0.1757	*	4.890	1.00
O1	$\frac{1}{2}$	0	0	0.75(4)	2.041	1.00
	$\frac{1}{2}$	0	0	*	2.042	1.00
	$\frac{1}{2}$	0	0	*	2.001	0.875(5)
	$\frac{1}{2}$	0	0	*	2.059	1.00
O2	0.1710(5)	0.3420(5)	0.3244(8)	0.75(4)	2.065	1.00
	0.1713(12)	0.3426(12)	0.3242(9)	*	2.071	1.00
	0.1717(17)	0.3434(17)	0.3225(25)	*	2.116	0.875(5)
	0.1744	0.3487	0.3256	*	2.087	1.00

The first line is a fully B-site ordered refinement, the second line corresponds a "B anti-site" refinement (see text) while the third line corresponds to a stacking faulted refinement (again see text). The last line shows the starting values given in [2]. All standard deviations have been multiplied with 2.15, 2.23 and 2.43, respectively (as recommended in [17] and references contained therein).
$a = 5.7698(8)$ Å and $c = 7.0855(9)$ Å (neutrons).
$a = 5.7737(4)$ Å and $c = 7.0852(9)$ Å (X-ray [2]).

correlation existed in the refinement and that the output standard deviations should therefore be multiplied by 2.15 (see [17] and references therein). The final refined structural parameters and resulting bond valence sum (or apparent valence—AV [18]) values are given in Table 1. The former are in reasonably good agreement with the predicted starting model [2]. The resultant profile fit is shown in Fig. 1a while the refined crystal structure is shown in projection down the $\mathbf{b}_h$ axis in Fig. 2a. The projected unit cell (shown outlined) is rotated in order to facilitate comparison with the refined crystal structure of $Ca_3CoNb_2O_9$ shown in Fig. 2b (see below).

3.2.2. "B-site disordered" refinement

There have been numerous reports in the literature about B-site disorder in these $P\bar{3}m1$, $A_3^{2+}(B^{2+}M_2^{5+})O_9$ types of perovskites (particularly for $M^{5+} = Nb$ compounds) and the effect that this has upon, in particular, microwave dielectric loss properties (see e.g. [5,11,19–21] and references contained therein). The prime evidence for B anti-site disorder is the experimental observation that the measured ratio of the integrated intensity of a low angle (and hence B-site occupancy sensitive) superstructure reflection $\left(\langle 100\rangle_h^*\right)$ to that of a nearby parent perovskite Bragg reflection $(\langle 110\rangle_p^*)$ is often observed to be variable (see e.g. Fig. 2 of [19]). This measured intensity ratio has even been used to define a so-called B site "… order parameter S …" [11] supposedly reflecting the degree of B^{2+}/M^{5+} ordering onto the $1b$ (B^{2+}) and $2d$ (M^{5+}) B-site positions of the $P\bar{3}m1$ superstructure space group symmetry. Given that the intensity of this low angle superstructure reflection is predominantly related to the extent of the B^{2+}/M^{5+} ordering onto the $1b/2d$ sites, the simplest way to alter this ratio from a Rietveld refinement point of view is simply to allow coupled partial occupancies on these two sites. Recent refinements of isostructural compounds to $Ba_3CoNb_2O_9$ have used such an "anti-site disorder" model [19,21] and hence refined the B^{2+}/M^{5+} ratio on each of the $1b$ and $2d$ sites (see e.g. Table 2 of [21]). Using the same occupancy constraints as Lufaso [21] (i.e., $Co_{1-2y}Nb_{2y}$ on the $1b$ site and Co_yNb_{1-y} on

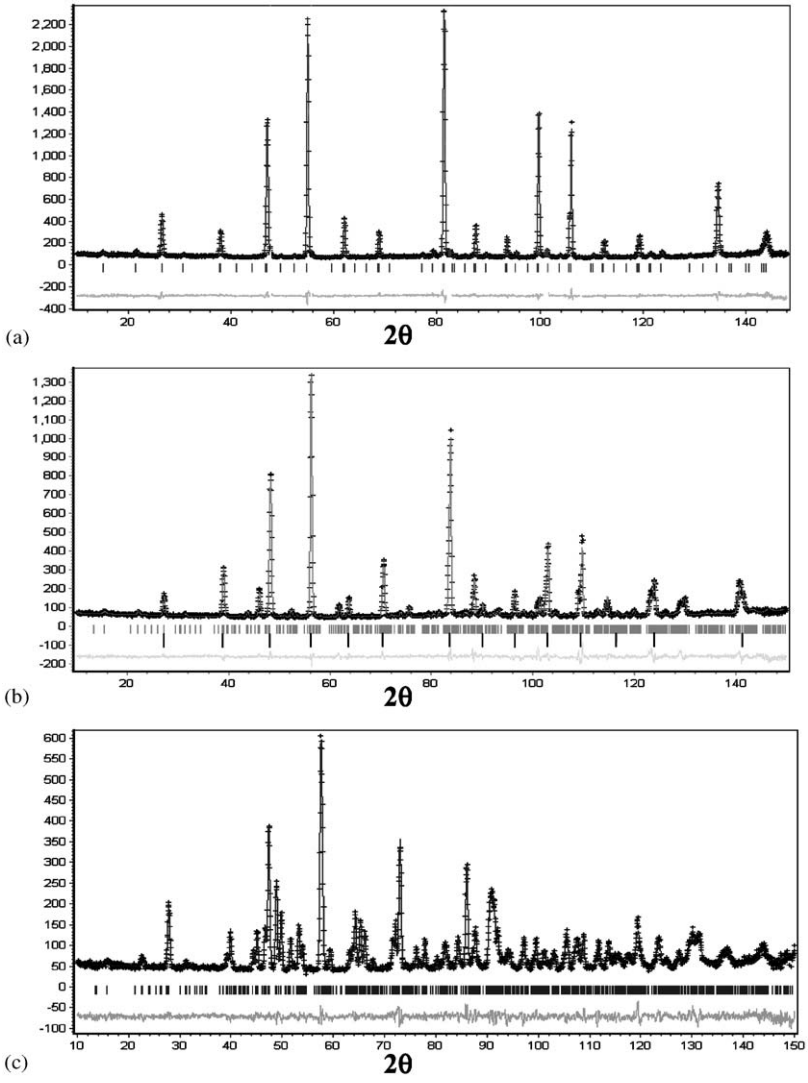

Fig. 1. Shows the experimental neutron powder diffraction patterns of (a) $Ba_3CoNb_2O_9$, (b) $Sr_3CoNb_2O_9$ and (c) $Ca_3CoNb_2O_9$ along with the final profile fits and difference plots.

the 2*d* site), an anti-site occupancy of Co^{2+} on the 2*d* site of ~4.19% and of Nb^{5+} on the 1*b* site of ~8.38% (see [21]) is obtained if the same approach is used here for $Ba_3CoNb_2O_9$ (see the second lines of fractional co-ordinates given in Table 1). The fractional co-ordinates and refinement statistics barely change.

The problem with such an approach, however, is that it is entirely unphysical. To simply switch an M^{5+} ion from the rather smaller 2*d* sites into the much larger 1*b* (B^{2+}) sites and/or vice-versa without altering the surrounding oxygen environment makes no crystal chemical commonsense at all as is readily apparent from simple bond valence sum considerations (see e.g. Table 2). Using, for example, the refined fractional co-ordinates in line 2 of Table 1, the calculated bond valence sum, or apparent valence (AV) [18], of the Nb^{5+} ion goes from the crystal chemically reasonable value of 4.748 when placed on the 2*d* position to the crystal chemically quite unreasonable value of 3.437 when placed on the 1*b* site while the AV of the Co^{2+} ion likewise changes from the crystal chemically reasonable value of 1.902 when placed on the 1*b* position to the crystal chemically quite unreasonable value of 2.627 when placed on the 2*d* position. At the same time, the AVs of the two O^{2-} ions are also quite negatively affected by any such changes (see Table 2). Similarly implausible bond valence sums are obtained upon the introduction of "anti-site disorder" for both $Ba_3ZnNb_2O_9$ and $Ba_3NiNb_2O_9$ if the recently refined fractional co-ordinates of Lufaso [21] are used. Clearly the "anti-site" disorder refinement approach does not appropriately model the local chemical reality and an alternative approach to *B*-site disorder is needed.

HREM lattice images of $Ba_3CoNb_2O_9$ (such as that shown in Fig. 3) strongly suggest that the apparent *B*-site disorder in these perovskite related superstructure

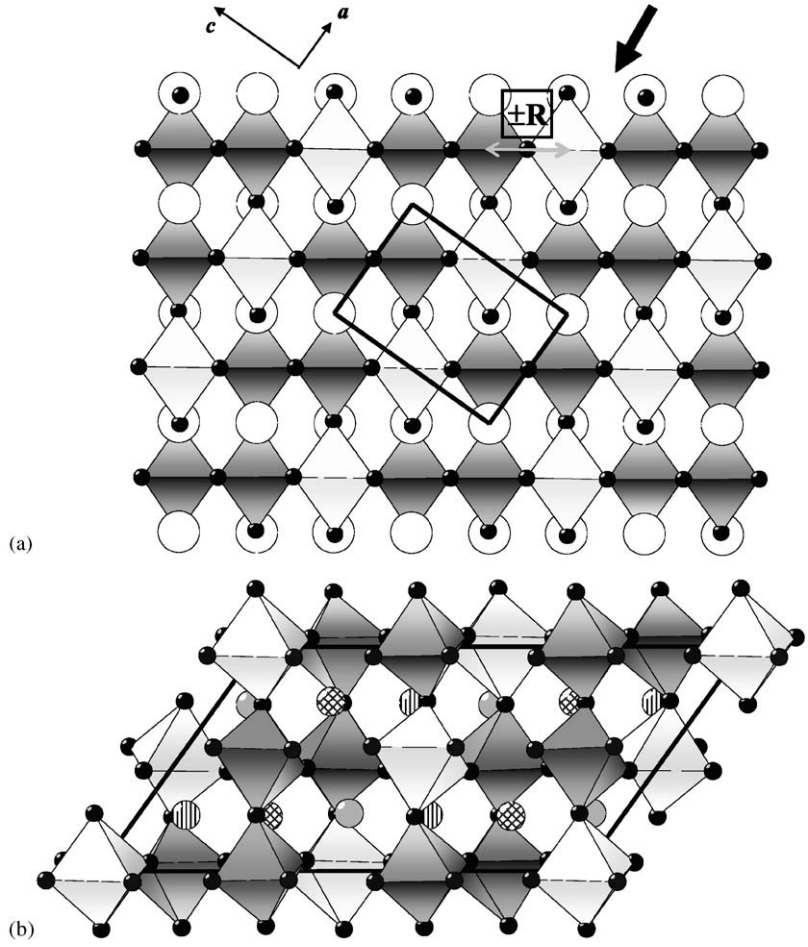

Fig. 2. Shows the final refined crystal structures of (a) $Ba_3CoNb_2O_9$ in projection down the $\mathbf{b}_h$ axis and (b) $Ca_3CoNb_2O_9$ in projection down the $\mathbf{b}_m$ axis. The projected unit cells are outlined in each case and are oriented to facilitate comparison between the two crystal structures. The darker octahedra represent NbO_6 octahedra while the lighter octahedra represent CoO_6 octahedra in each case. The largest balls represent Ba ions in the case of (a) and Ca ions in the case of (b).

Table 2
Calculated bond valence sums, or AV's, for $Ba_3CoNb_2O_9$ using the refined fractional co-ordinates of Table 1 and allowing for coupled anti-site disorder

AV	Co in 1*b*, Nb in 2*d* Prob. = 0.8779	Nb in 1*b*, Nb in 2*d* Prob. = 0.0803	Co in 1*b*, Co in 2*d* Prob. = 0.0384	Nb in 1*b*, Co in 2*d* Prob. = 0.0035
Ba1	2.471	2.471	2.471	2.471
Ba2	2.340	2.340	2.340	2.340
Co/Nb in *1b*	1.902	3.437	1.902	3.437
Nb/Co in 2d	4.748	4.748	2.627	2.627
O1	2.042	2.042	1.478	1.478
O2	2.071	2.327	1.645	1.901

The respective probabilities are calculated using $y = 0.0419$ (see text).

phases has nothing to do with genuine "anti-site" disorder but rather reflects the existence of microstructure, in particular translational stacking faulting (characterized by a displacement shift vector of the whole superstructure across stacking faults of $\pm\mathbf{R}$, where $\mathbf{R} \sim \mathbf{c}_p \equiv \frac{1}{3}[-\mathbf{a}_h + \mathbf{b}_h + \mathbf{c}_h]$) within individual $P\bar{3}m1$ orientational domains. One such stacking fault is apparent from sighting along the direction of the black arrow shown in Fig. 3b. The same direction is represented by the thick black arrow in Fig. 2a. Such translational stacking faulting, as well as the rotational twinning also clearly present in Fig. 3 (whereby the supercell $\mathbf{c}_h$ axis

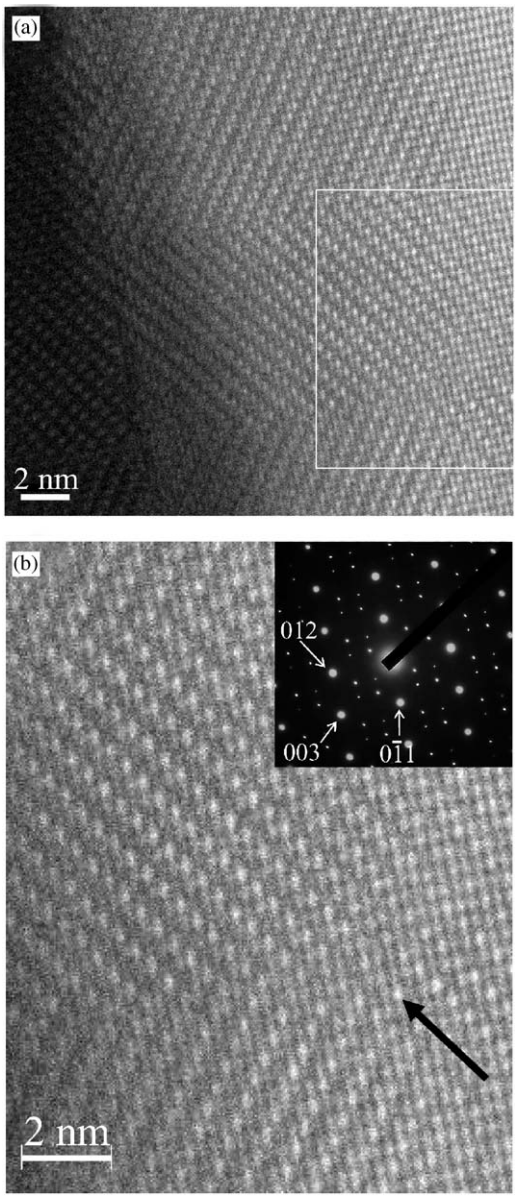

Fig. 3. HREM lattice image of $Ba_3CoNb_2O_9$ down the [100] direction showing both rotational twinning as well as stacking faulting: (a) shows a wider angle view while (b) shows a blow-up of the area in the white box of (a). The associated EDP is inset. A stacking fault in the hexagonal superstructure is apparent by sighting along the black arrow.

flips from one parent perovskite $\langle 111 \rangle_p$ direction to another), are only to be expected given the relationship between the superstructure unit cell and space group symmetry and that of the underlying perovskite type parent structure. Since, however, the local crystal structure is the same on either side of any such stacking faults, so is the local chemistry and hence the local bond valence sums (except in the immediate vicinity of the fault itself).

From the Rietveld refinement point of view, the effect of a displacive shift by $\pm\mathbf{R}$ (also shown in Fig. 2a) is to introduce apparent *B*-site disorder (see Fig. 2a). Note, however, that this is *not* the same thing as anti-site substitution. To easily test for this, however, is not an option in either of the programs used in the refinements and an alternative approach had to be developed.

Table 3
The fractional co-ordinates of the three (*a*, *b* and *c*) translation variants used to simulate the effect of translation stacking faults on the $Ba_3CoNb_2O_9$ structure

Atom	*x*	*y*	*z*
$Ba1_a$	0	0	0
$Ba1_b$	$\frac{1}{3}$	$\frac{2}{3}$	$0-\frac{1}{3}-\delta$
$Ba1_c$	$\frac{2}{3}$	$\frac{1}{3}$	$0+\frac{1}{3}+\delta$
$Ba2_a$	$\frac{1}{3}$	$\frac{2}{3}$	z(Ba2)
$Ba2_b$	$\frac{2}{3}$	$\frac{1}{3}$	z(Ba2) $-\frac{1}{3}-\delta$
$Ba2_c$	0	0	z(Ba2) $+\frac{1}{3}+\delta$
$Ba2'_a$	$\frac{2}{3}$	$\frac{1}{3}$	$-z$(Ba2)
$Ba2'_b$	0	0	$-z$(Ba2) $-\frac{1}{3}-\delta$
$Ba2'_c$	$\frac{1}{3}$	$\frac{2}{3}$	$-z$(Ba2) $+\frac{1}{3}+\delta$
Co_a	0	0	$\frac{1}{2}$
Co_b	$\frac{1}{3}$	$\frac{2}{3}$	$\frac{1}{2}-\frac{1}{3}-\delta$
Co_c	$\frac{2}{3}$	$\frac{1}{3}$	$\frac{1}{2}+\frac{1}{3}+\delta$
Nb_a	$\frac{1}{3}$	$\frac{2}{3}$	z(Nb)
Nb_b	$\frac{2}{3}$	$\frac{1}{3}$	z(Nb) $-\frac{1}{3}-\delta$
Nb_c	0	0	z(Nb) $+\frac{1}{3}+\delta$
Nb'_a	$\frac{2}{3}$	$\frac{1}{3}$	$-z$(Nb)
Nb'_b	0	0	$-z$(Nb) $-\frac{1}{3}-\delta$
Nb'_c	$\frac{1}{3}$	$\frac{2}{3}$	$-z$(Nb) $+\frac{1}{3}+\delta$
$O1_a$	$\frac{1}{2}$	0	0
$O1_b$	$\frac{1}{2}+\frac{1}{3}$	$0+\frac{2}{3}$	$0-\frac{1}{3}-\delta$
$O1_c$	$\frac{1}{2}-\frac{1}{3}$	$0+\frac{1}{3}$	$0+\frac{1}{3}+\delta$
$O2_a$	x(O2)	2x(O2)	z(O2)
$O2_b$	x(O2) $+\frac{1}{3}$	2x(O2) $+\frac{2}{3}$	z(O2) $-\frac{1}{3}-\delta$
$O2_c$	x(O2) $+\frac{2}{3}$	2x(O2) $+\frac{1}{3}$	z(O2) $+\frac{1}{3}+\delta$
$O2'_a$	$-x$(O2)	$-2x$(O2)	$-z$(O2)
$O2'_b$	$-x$(O2) $+\frac{1}{3}$	$-2x$(O2) $+\frac{2}{3}$	$-z$(O2) $-\frac{1}{3}-\delta$
$O2'_c$	$-x$(O2) $+\frac{2}{3}$	$-2x$(O2) $+\frac{1}{3}$	$-z$(O2) $+\frac{1}{3}+\delta$

Three translational variants of the superstructure were thus created (labelled with the subscripts *a*, *b* and *c* respectively in Table 3). The fractional co-ordinates of the dominant translational variant are labelled with the subscript *a* in Table 3 while those of the minor translation variants (corresponding to the identical superstructure but translated by $-\mathbf{R}$ and $+\mathbf{R}$ respectively, where $\mathbf{R} = [-\frac{1}{3}, \frac{1}{3}, \frac{1}{3}+\delta]_h$) are labelled with the subscripts *b* and *c* respectively in Table 3. The only additional variables to refine in this "*B*-site disordered" refinement are the relative occupancies of the *a*, *b* and *c* translation variants along with the parameter δ. *P*3*m*1 space group symmetry was first of all assumed to allow for the possibility that the occupancies of the *b* and *c* variants might not be equal. The refinement, however, showed no preference for either the *b* or *c* variant over the other so that their occupancies were subsequently constrained to be equal. Note that equal occupancy of

the b and c translational variants restores the inversion center and the overall $P\bar{3}m1$ space group symmetry (see Table 3). Due to the high correlation between ADPs, occupancies, peak profile parameters and atomic positions, the ADPs were locked to their originally refined values as given in Table 1.

The refinement converged rapidly. The occupancies of the a, b and c translation variants refined to 0.875(5), 0.063(5) and 0.063(5), respectively, while the parameter δ refined to $-0.023(12)$. The third lines of fractional co-ordinates in Table 1 gives the final refined fractional co-ordinates of the a variant. Again the refined fractional co-ordinates and refinement statistics barely changed from those of the fully ordered refinement (see Table 1).

Even though most of the additional parameters could (in this case) be coupled and the original space group maintained, the introduction of stacking faults clearly complicates the structure description, quite possibly beyond what the available data might allow to be refined. As a consequence this type of modelling was only attempted for the $Ba_3CoNb_2O_9$ structure and not for the other two compounds investigated in this study.

3.3. $Ca_3CoNb_2O_9$

The $P12_1/c1$, $\mathbf{a}_m = [\bar{1}\bar{1}2]_p$, $\mathbf{b}_m = [1\bar{1}0]_p$, $\mathbf{c}_m = 3[110]_p$ ($\mathbf{a}^*_m = \frac{1}{2}[001]^*_p$, $\mathbf{b}^*_m = \frac{1}{2}[1\bar{1}0]^*_p$, $\mathbf{c}^*_m = \frac{1}{6}[111]^*_p$) perovskite-related supercell of the $Ca_3CoNb_2O_9$ compound is rather more complicated and contains 16 independent atoms, all of which are on general positions except for two Co-ions which are on fixed positions (see [2]). Formally, there are therefore $14 \times 3 = 42$ fractional co-ordinates to be derived/refined (33 associated with the octahedral framework portion of the structure and nine with the interstitial Ca ions), no mean feat from powder diffraction data.

The same four unknown displacive parameters, ε_O, ε'_O, ε_{Nb} and ε_A, corresponding to the displacive shifts accompanying the Co^{2+}/Nb^{5+} ordering and associated with the modulation wave-vector $\mathbf{q} = \frac{1}{3}[111]^*_p$, described above for the $A = Ba$ compound remain for the $A = Ca$ compound. In addition, however, there now exist potential extra displacive degrees of freedom associated with each of the new modulation wave-vectors $\mathbf{q}$ giving rise to the additional observed satellite reflections at $\mathbf{G} \pm \mathbf{q}$ ($\mathbf{G}$ a parent perovskite sub-structure reflection) in the case of the $A = Ca$ compound (see e.g. Fig. 4 of [2]). Formally there are six additional modulation wave-vectors accompanying the $\mathbf{q} = \frac{1}{3}[111]^*_p$ modulation associated with the $A = Ca$ compound i.e., $\frac{1}{2}[111]^*_p$, $\frac{1}{2}[110]^*_p$, $\frac{1}{6}[111]^*_p$, $\frac{1}{6}[\bar{2}\bar{2}1]^*_p$, $\frac{1}{6}[\bar{1}\bar{1}2]^*_p$ and $\frac{1}{2}[001]^*_p$, respectively.

By far the strongest of these additional satellite reflections are associated with the modulation wave-vectors $\frac{1}{2}[111]^*_p$ and $\frac{1}{2}[110]^*_p$ (see [2]) thus suggesting that only the additional displacive degrees of freedom associated with these modulation wave-vectors need to be included in order to obtain a good first approximation to the structure of the $A = Ca$ compound. If in addition the crystal chemically reasonable assumption that these latter displacive degrees of freedom are primarily associated with CoO_6 and NbO_6 octahedral rotation alone (around the $[110]_p$ axis with an amplitude ε_{110} in the case of the $\mathbf{q} = \frac{1}{2}[111]^*_p$ modulation and around the $[001]_p$ axis with an amplitude ε_z in the case of the $\mathbf{q} = \frac{1}{2}[110]^*_p$ modulation), it is then possible to predict resultant fractional co-ordinates for all 16 independent atom sites in terms of only six unknown parameters, the above four parameters in conjunction with ε_{110} and ε_z (see Table 3 of [2]). Furthermore, crystal chemical/bond valence sum considerations can then be used to obtain expected values for each of these parameters (see Table 6 of [2]). This drastically reduces the number of free parameters to be refined as well as providing good starting fractional co-ordinates for the refinement.

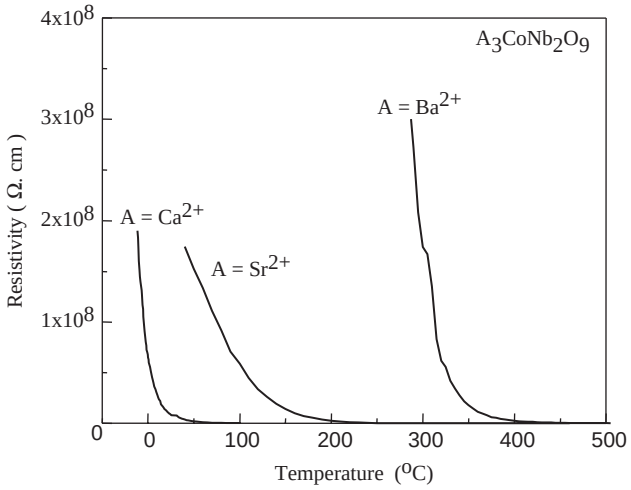

Fig. 4. Measured temperature dependence of the electrical resistivity of the three $A_3CoNb_2O_9$, A = Ca, Sr and Ba, complex perovskite samples.

The refinement was first of all allowed to progress without any constraints at all. This initial refinement converged quickly and gave the best possible fit to the experimental data (see below) but quite poor local crystal chemistry as judged by bond valence sum considerations [18]. This strongly suggested that an unconstrained approach to Rietveld refinement was very unlikely to lead to a plausible resultant crystal structure and that a significant reduction in the number of nominally independent refineable variables (including fractional co-ordinate variables) via appropriate constraints was absolutely necessary. Under these conditions, it was clearly inappropriate to refine individual ADPs. The ADPs of the O ions were thus thereafter constrained to be the same as were the ADPs of the Ca ions as well as the ADPs of the Co and Nb ions.

The obtained refinement statistics of this initial unconstrained refinement (based on the Rietica

program) were R_p: 6.05, R_{wp}: 7.39, χ^2: 2.29 and R_{Bragg}: 2.32 with D-W *d*-statistics parameters of 1.00/1.90 using a total of 62 parameters for 861 theoretical Bragg reflections. By comparing these refined fractional co-ordinates with the predicted fractional co-ordinates in Table 3 of [2], average values for the displacement parameters, ε_{Nb}, ε_{110}, ε_O, ε'_O and ε_z were extracted. These average values were then re-entered into Table 3 of [2] to give new starting fractional co-ordinate values. The respective displacement parameters, ε_{Nb}, ε_{110}, ε_O, ε'_O and ε_z, were then each individually refined in such a way that only the atomic co-ordinates dependent upon a particular displacement parameter were refined in turn, starting with the displacement parameter with the largest nominal value. This was repeated until the refinement converged.

The best refinement statistics obtained with this approach (using FULLPROF) were R_p: 8.87, R'_{wp}: 11.90, χ^2: 5.95 and R_{Bragg}: 16.40. By far the largest amplitude atomic shifts were associated with the octahedral rotation around $[110]_p$ mode (corresponding to the ε_{110} parameter) and the octahedral rotation around $[001]_p$ mode (corresponding to the ε_z parameter) as expected. While this refined structure gave excellent bond valence sum (or apparent valence, AV) values, it clearly did not model the observed diffraction pattern well enough. It was clear that additional terms needed to be added in order to more closely model the observed diffraction data.

Going back to the initial unconstrained refinement, it became clear that the missing displacive degrees of freedom were associated with $\mathbf{c}_m$ shifts of the apical O3, O8 and O9 oxygens (see Table 4) as well as the Ca-cations. Given the resultant space group symmetry, such shifts could only be associated with the modulation wave-vectors $\frac{1}{2}[001]^*_p$ and $\frac{1}{6}[\bar{2}\bar{2}1]^*_p$. Both modulation wave-vectors only allow $\mathbf{c}_m$ shifts of the apical O3, O8 and O9 ions. Clearly such motion will distort somewhat the shape of the previously essentially regular octahedra. In addition one further parameter, ε'_z, allowing for the possibility of octahedral rotation around $[001]_p$ associated with the modulation wave-vector $\frac{1}{2}[111]^*_p$ was also allowed. Each of these additional parameters was then individually refined in the same manner as described above leading to a considerable improvement in refinement statistics. Finally displacements of the Ca ions away from their parent perovskite positions were also allowed.

At this stage, the refinement rapidly converged to give refinement statistics virtually identical to the totally unconstrained refinement but now with excellent local crystal chemistry. The obtained refinement statistics, using both Rietica and (FULLPROF) were R_p: 6.17/(6.06), R_{wp}: 7.51/(7.45), χ^2: 2.33/(2.33) and R_{Bragg}: 2.23/(5.03) with D-W *d*-statistics parameters of 1.01/1.90 indicating that the output standard deviations should be multiplied by 1.847 (see [17] and references therein). The number of variables used was 29 (as opposed to 62 for a totally unconstrained refinement) for 861 theoretical reflections. The final refined atomic co-ordinates, unit cell parameters and AVs are given in Table 4 and the profile fit in Fig. 1c. The obtained epsilon parameters (cf. with Table 5 of [2]) were (starting values from [2] in brackets): ε_{Nb}~0.0092 (0.0102), ε_{110}~0.0956 (0.096), ε_O~0.0031, $\varepsilon'_O \sim 0.0086$ ($\varepsilon_O = \varepsilon'_O \sim 0.0064$), ε_z~0.0472 (0.048), $\varepsilon'_z \sim 0.0064$ (defined as 0), $\varepsilon_z(\frac{1}{2}[001]^*_p)$~0.0088 (defined as 0) and $\varepsilon_z(\frac{1}{6}[\bar{2}\bar{2}1]^*_p)$~0.0024 (defined as 0).

The fractional co-ordinates obtained using the above constrained refinement approach are necessarily coupled and thus errors are underestimated. To test the accuracy of the obtained structure, each of the refined fractional co-ordinates were thus allowed to vary individually while the rest were held fixed. The differences from the listed values (Table 4) did not deviate by more than 2 standard deviations.

3.4. $Sr_3CoNb_2O_9$

The refinement strategy used for the Sr compound was the same as that used for the analogous Ca compound described above. The structure was thus initially allowed to refine without constraints and the initial magnitude of the relevant shift vectors (see [2]) obtained as the average of the difference between the refined values and the starting values. As was the case for the Ca compound, additional shift vectors were needed which distorted the octahedra somewhat. The best refinement obtained with this approach was as follows (the unconstrained refinement in brackets and all data using Rietica) R_p: 6.64/(6.04), R_{wp}: 8.73/7.68), χ^2: 3.68/(2.88) and R_{Bragg}: 3.92/(2.92) using 24/(62) parameters in total for the 922 theoretical reflections.

During this refinement process, however, it was realized that some of the high angle parent perovskite peaks could not be well fitted irrespective of the refinement approach. It was realized that this must originate in something that was not directly dependent on the local atomic arrangement in the structure, such as preferred orientation, strain effects, micro-twinning, stacking faulting (see e.g. Fig. 3) or the possibility of an additional contamination phase whose peak positions overlapped strongly with the lines from $Sr_3CoNb_2O_9$. This latter approach seemed the most likely since the effect we could see in the refinement was that some of the parent reflections in the high angle part of the pattern were systematically under-calculated.

A very recent study by Bieringer et al. [19] of $Ba_3ZnTa_2O_{9-\delta}$ (essentially isomorphous to the $Ba_3CoNb_2O_9$ compound but closely related to the $Sr_3CoNb_2O_9$ compound) reported that the formation of a disordered cubic perovskite contamination phase is likely to occur in uncovered samples of such complex

Table 4
Structural parameters and the resulting apparent valence (AV) values obtained for the refinement of $Ca_3CoNb_2O_9$ all standard deviations from the output have been multiplied with 1.847

Atom	x	y	z	B	AV
Co1	0	0	0	0.44(10)	2.002
	0	0	0	—	2.024
Co2	$\frac{1}{2}$	$\frac{1}{2}$	0	0.44(10)	2.023
	$\frac{1}{2}$	$\frac{1}{2}$	0	—	2.024
Nb1	0.5046(9)	0.5000	0.3377(9)	0.44(10)	4.983
	0.5051	0.5000	0.3385	—	5.040
Nb2	0.0046(9)	0.0000	0.3377(9))	0.44(10)	4.983
	0.0051	0.0000	0.3385	—	5.040
$Ca1_1$	0.258(2)	0.480(4)	0.0068(9)	0.64(12)	1.944
	0.2500	0.5000	0.0833	—	2.026
$Ca1_2$	0.750(2)	-0.015(4)	0.0098(9)	0.64(12)	1.975
	0.7500	0.0000	0.0833	—	2.025
Ca2	0.245(2)	0.005(4)	0.2300(9)	0.64(12)	1.998
	0.2500	0.0000	0.2500	—	2.028
O1	0.9571(17)	0.7051(31)	0.2506(9)	0.53(8)	1.961
O11	0.9520	0.7020	0.2500	—	2.013
O2	0.5408(18)	0.7939(30)	0.2783(9)	0.53(8)	2.005
O12	0.5480	0.7980	0.2820	—	2.012
O3	0.2500(21)	0.5930(23)	0.2564(7)	0.53(8)	2.041
O13	0.2500	0.5960	0.2500	—	2.013
O4	0.9521(17)	0.6934(29)	0.9125(9)	0.53(8)	1.894
$O21_1$	0.9520	0.6924	0.9135	—	2.025
O5	0.0387(17)	0.1956(29)	0.9065(9)	0.53(8)	2.030
$O21_4$	0.0480	0.2116	0.9135	—	2.001
O6	0.4450(18)	0.2800(28)	0.8802(9)	0.53(8)	1.927
$O21_2$	0.4520	0.2884	0.8815	—	2.045
O7	0.5512(7)	0.7997(29)	0.9453(9)	0.53(8)	2.008
$O21_3$	0.5480	0.8076	0.9455	—	2.025
O8	0.7425(20)	0.0930(23)	0.9072(7)	0.53(8)	1.999
$O23_1$	0.7404	0.0960	0.9135	—	2.025
O9	0.2425(20)	0.5930(23)	0.9272(7)	0.53(8)	2.030
$O23_2$	0.2404	0.5960	0.9135	—	2.025

The second line is the starting values given in [2]. See text for details.
$a = 9.596(2)$ Å, $b = 5.4619(5)$ Å, $c = 16.829(2)$ Å and $\beta = 125.70(1)^\circ$.
$a = 9.5985(6)$ Å, $b = 5.4685(4)$ Å, $c = 16.8094(9)$ Å and $\beta = 125.719(4)^\circ$ [2].

perovskite materials when heated at 1350 °C. Such a contaminant phase could be expected to have its strongest diffraction lines at the same or very similar positions to the parent lines of the majority $Sr_3CoNb_2O_9$ compound and hence would be very difficult to observe. Thus it seemed at least plausible that such a 'phase' could have formed and gone undetected during the synthesis and characterization stage of this study. (Note that micro-twinning and stacking faulting of the type shown in Fig. 3 for $Ba_3CoNb_2O_9$ could well be expected to lead to what would be seen by powder diffraction as a disordered cubic 'phase' if it occurred on a fine enough scale. Given the complexity of the crystal structure, however, it was not feasible to model this along the lines of Sn.3.2.2).

To test this hypothesis a second disordered cubic phase was thus added to the refinement. The cell parameter, $a_{\text{cubic}} \sim 3.996$ Å, was chosen so as to put additional intensity into the under-calculating parent perovskite reflections (see Fig. 1b) while the atomic

Table 5
Structural parameters and the resulting apparent valence (AV) values obtained for the refinement of $Sr_3CoNb_2O_9$ using a two-phase model (see text for details), all standard deviations have been multiplied with 2.25

Atom	x	y	z	B	AV
Co1	0	0	0	0.52(9)	2.056
	0	0	0	—	2.024
Co2	$\frac{1}{2}$	$\frac{1}{2}$	0	0.52(9)	1.984
	$\frac{1}{2}$	$\frac{1}{2}$	0	—	2.024
Nb1	0.5040(11)	$\frac{1}{3}$	0.3373(11)	0.52(9)	4.918
	0.5050	0.5000	0.3383	—	5.040
Nb2	0.0040(11)	$\frac{1}{3}$	0.3373(11)	0.52(9)	5.084
	0.0050	0.0000	0.3383	—	5.040
$Sr1_1$	0.2500	0.0000	0.0833	1.19(9)	1.909
	0.2500	0.5000	0.0833	—	2.026
$Sr1_2$	0.7500	0.0000	0.0833	1.19(9)	2.103
	0.7500	0.0000	0.0833	—	2.025
Sr2	0.2500	0.0000	0.2500	1.19(9))	2.066
	0.2500	0.0000	0.2500	—	2.028
O1	0.9720(24)	0.7425(56)	0.2432(16)	0.81(8)	2.029
O11	0.9740	0.7240	0.2500	—	2.013
O2	0.5260(38)	0.7871(65)	0.2716(16)	0.81(8)	2.044
O12	0.5260	0.7760	0.2673	—	2.012
O3	0.2500(45)	0.5428(51)	0.2626(18)	0.81(8)	2.040
O13	0.2500	0.5520	0.2500	—	2.013
O4	0.9721(38)	0.7330(54)	0.9067(15)	0.81(8)	1.985
$O21_1$	0.9740	0.7146	0.9135	—	2.025
O7′	0.0279(37)	0.2518(49)	0.9202(16)	0.81(8)	2.000
$O21_4$	0.0266	0.2666	0.9135	—	2.025
O5	0.4721(39)	0.2777(49)	0.8919(17)	0.81(8)	1.985
$O21_2$	0.4740	0.2666	0.8962	—	2.001
O6′	0.5279(38)	0.7965(66)	0.9352(16)	0.81(8)	2.023
$O21_3$	0.5260	0.7146	0.4309	—	2.045
O8	0.7406(46)	0.0428(50)	0.9110(22)	0.81(8)	2.000
$O23_1$	0.7406	0.0520	0.9135	—	2.025
O9	0.2406(43)	0.5428(48)	0.9078 (22)	0.81(8)	1.996
$O23_2$	0.2406	0.5520	0.9135	—	*2.025*

The second line is the starting values given in [2].
$a = 9.7818(13)$ Å, $b = 5.6403(7)$ Å, $c = 17.005(2)$ Å and $\beta = 125.253(4)$ Å.
$a = 9.7828(7)$ Å, $b = 5.6429(5)$ Å, $c = 16.980(2)$ Å and $\beta = 125.205(7)$ Å. [7]

positions were set to the ideal parent perovskite positions. The occupancy of the B site was set to be $\frac{1}{3}$Co and $\frac{2}{3}$Nb, i.e., randomly distributed, while the thermal parameters were set to be identical to those of the main phase. The only additional parameters thus added were a new scale factor for this second phase and its unit cell parameter. This indeed improved the refinement statistics and took care of some of the problems encountered in the initial refinement process.

The final refinement statistics for $Sr_3CoNb_2O_9$ utilizing both Rietica and (FULLPROF) were R_p: 6.16/(6.12), R_{wp}: 7.84/(7.86), χ^2: 2.97/(3.03) and R_{Bragg}: 2.95/(9.36) using 31 parameters in total for the 922 theoretical reflections. The Durbin-Watson d-statistics parameters were 0.80/1.90 indicating that the output standard deviations should be multiplied by 2.25, largely due to a greater problem with overlapping reflections in the case of the Sr compound as compared to the Ca-analogue compound (cf. Figs. 1b and c). The final refined structural parameters are given in Table 5 and the diffraction profile fit shown in Fig. 1b. The obtained epsilon parameters (cf. with Table 3 of [2]) were (starting values from [2] in brackets): ε_{Nb}∼0.0080 (0.0100), ε_{110}∼0.0537 (0.052), ε_O∼0.0061, $\varepsilon'_O \sim 0.0061$($\varepsilon'_O = \varepsilon_O =$ 0.0063), ε_z∼0.0223 (0.026), $\varepsilon'_z \sim 0.0144$ (not considered

in [2] i.e., effectively defined as 0), $\varepsilon_z(\frac{1}{2}[001]^*_p) \sim 0.0031$ (not considered in [2] i.e., effectively defined as 0) and $\varepsilon_z(\frac{1}{6}[\bar{2}\bar{2}1]^*_p) \sim -0.0095$ (not considered in [2] i.e., effectively defined as 0). The phase fraction percentage of the disordered cubic phase refined to 14(1)%.

3.5. Physical properties

3.5.1. Electrical resistivity

Fig. 4 shows the measured temperature dependence of the electrical resistivity of each of the three $A_3CoNb_2O_9$ complex perovskite samples. A well-defined semiconductor to insulator transition is apparent in all three samples with transition temperatures of ~325, 126 and 8 °C for $A = Ba^{2+}$, Sr^{2+} and Ca^{2+}, respectively. These transition temperatures could reasonably be expected to correlate with the average transition metal-transition metal separation distances, which in turn will correlate with the amplitude of the octahedral rotation modes through their effect upon the average parent perovskite unit cell volume. The observed transition temperatures are consistent with such an expectation.

The $8.3 \times 10^6\,\Omega$ cm room temperature resistivity of the $A = Ca$ compound is characteristic of a semiconductor while that of the $A = Ba$ compound is typical of an insulator. The room temperature resistivity of the $A = Sr$ compound takes an intermediate value between these two extremes.

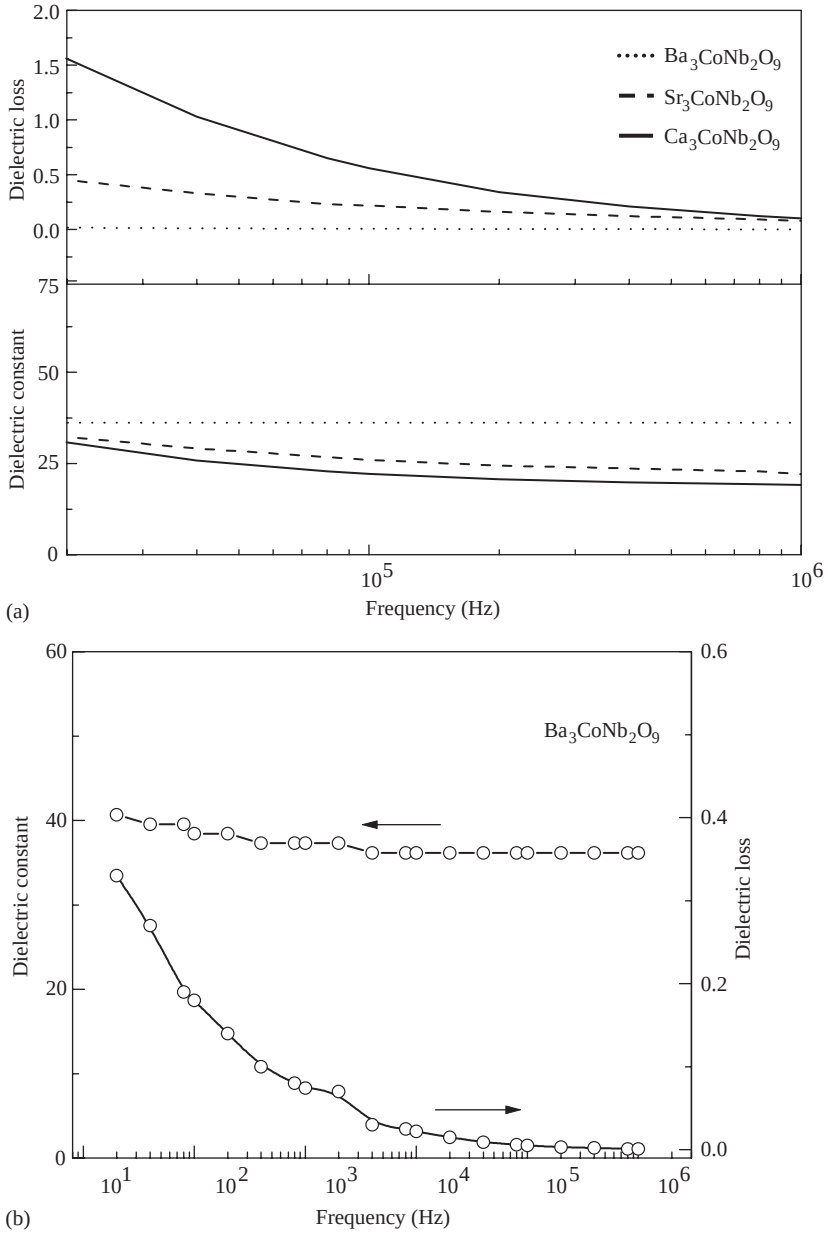

Fig. 5. (a) Dielectric frequency characteristics of the $A_3CoNb_2O_9$, $A = Ca$, Sr and Ba, compounds at room temperature. (b) A considerably expanded plot of these characteristics for the $A = Ba$ compound.

The semiconductor to insulator transition of both $Ca_3CoNb_2O_9$ and $Ba_3CoNb_2O_9$ is quite steep as a function of temperature, while the curve for the $Sr_3CoNb_2O_9$ compound shows a rather more gradual change. (This may be indicative of the presence of a disordered cubic contaminant phase in the case of the Sr compound). In the semiconducting range, the temperature dependence of the conductivity, $\sigma = 1/\rho$, can be fitted via the equation $\sigma = C\exp(E_a/kT)$, where C is a constant, k is the Boltzmann constant, and E_a is an activation energy. The gap, E_a, is thereby calculated to be 0.19 eV for the A = Ba compound, 0.13 eV for the A = Sr compound and 0.07 eV for the A = Ca compound. The higher activation energy for the A = Ba compound results in a higher insulator to semiconductor transition temperature.

3.5.2. Dielectric properties

Fig. 5a shows the measured dielectric frequency characteristics of each of the three compounds at room temperature for frequencies from 20 kHz up to 1 MHz, while Fig. 5b shows a considerably expanded plot of these characteristics for the A = Ba compound. $Ba_3CoNb_2O_9$ has a relatively high dielectric constant (~36) at 1 MHz and the lowest (closest to zero) dielectric loss. Ahn et al. [7] report a dielectric constant of 32 at

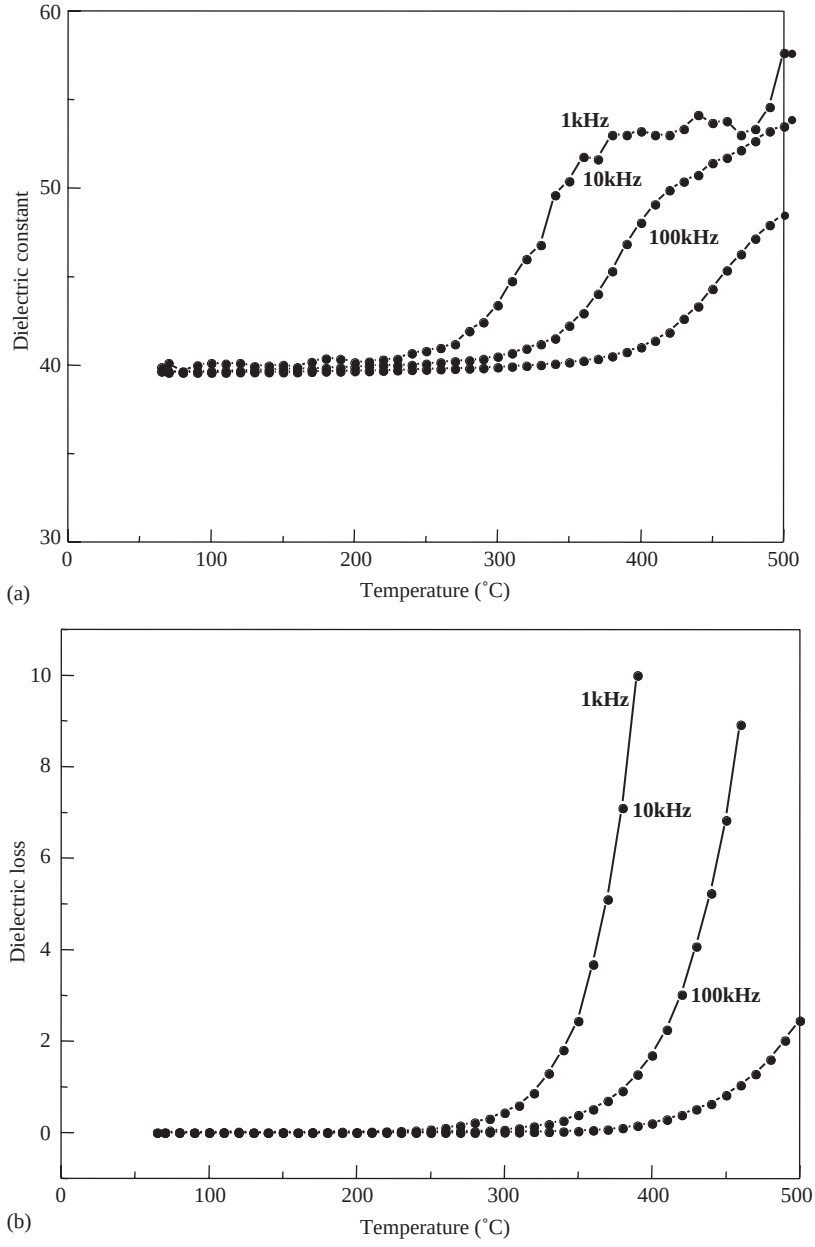

Fig. 6. Dielectric frequency characteristics of the $Ba_3CoNb_2O_9$ compound as a function of temperature at three different frequencies.

9 GHz for $Ba_3CoNb_2O_9$ while Molodetsky and Davies [6] report a dielectric constant of 32.9 at 8.6 GHz for "fully ordered" $Ba_3CoNb_2O_9$ and a dielectric constant of 35.7 at 8.6 GHz for a "disordered" $Ba_3CoNb_2O_9$. As is well known [4,6–8], the measured dielectric frequency characteristics of this $A = Ba$ compound at microwave frequencies [4,6–8] are excellent and hold promise for the practical application of this material. On the other hand, the dielectric constants of both the $Ca_3CoNb_2O_9$ and $Sr_3CoNb_2O_9$ compounds show an undesirable decrease with increasing frequency while the dielectric losses are quite high in the low frequency range since they are either undergoing a transition into a semiconducting state in the case of the $A = Sr$ compound or already in a semiconducting state in the case of the $A = Ca$ compound.

In the low frequency range, the majority of conducting defects can presumably follow the change in direction of the applied electric field leading to a large leakage current and thereby giving rise to a higher dielectric loss. As frequency increases, this is increasingly no longer true. Hence dielectric loss tends to decrease with increasing frequency. When the frequency increases close to 1 MHz, the dielectric losses of both the $A = Sr$ and Ca compounds converge at a reasonably small value (see Fig. 5a) while their dielectric constants also converge but at a significantly smaller value than that for $Ba_3CoNb_2O_9$.

As shown by Reaney et al. [22], non-octahedrally tilted, higher symmetry, complex perovskites (associated with tolerance factors $> \sim 1$, often with Ba ions in the perovskite A site) tend to have negative temperature coefficients of dielectric constant while octahedrally tilted complex perovskites (associated with lower tolerance factors, lower symmetry and with smaller Sr and/or Ca ions in the perovskite A site) tend to have positive temperature coefficients of dielectric constant. Experimentally, non-octahedrally tilted $Ba_3CoNb_2O_9$ has a desirable very small, essentially zero, positive temperature coefficient of dielectric constant ($\sim$30 ppm/K), giving rise to an essentially unchanged dielectric constant over a reasonably large temperature range as shown in Fig. 6. The measured temperature coefficient of the dielectric constant for $Ba_3CoNb_2O_9$ from room temperature to 300 °C is only 30 ppm/K, where the dielectric loss is always lower than 0.009. The dielectric constant and dielectric loss are 36 and 0.001 respectively at room temperature and 1 MHz frequency.

Such desirable characteristics suggests $Ba_3CoNb_2O_9$ has strong potential for use in dielectric devices, both at low frequency as well as at the previously reported microwave frequencies [4–8]. By contrast, when the Ba^{2+} cations in the perovskite A sites are replaced by the rather smaller Sr^{2+} and Ca^{2+} ions, the reduced tolerance factor leads to significant octahedral tilting and large (non-desirable) positive temperature coefficients of dielectric constant.

4. Conclusions

The structures of the $A_3CoNb_2O_9$triple perovskites have been determined by Rietveld refinement of neutron powder diffraction data using a constrained modulation wave approach. Non-octahedrally rotated $Ba_3CoNb_2O_9$ shows excellent dielectric properties that could potentially be of use in new microwave dielectric devices. The dielectric properties of the $A = Sr$ and Ca compounds, by contrast, are significantly degraded as a result of the lower tolerance factors and induced octahedral rotations. The insulator to semiconductor transitions in these compounds also occur at significantly lower temperatures than for the $A = Ba$ compound. The $Ca_3CoNb_2O_9$ compound is already a typical semiconductor at room temperature.

Acknowledgment

Financial support from the Australian Institute for Science and Engineering (AINSE), grant number AINGRA04173 is gratefully acknowledged. YL and RLW also gratefully acknowledge financial support from the Australian Research Council in the form of an ARC Discovery Grant.

References

[1] J. Yin, Z. Zou, J. Ye, J. Phys. Chem. B 107 (2003) 4936–4941.
[2] V. Ting, Y. Liu, R.L. Withers, L. Norén, J. Solid State Chem. 177 (2004) 2295–2304.
[3] H. Kagata, J. Kato, Jpn. J. Appl. Phys. 33 (1994) 5463–5465.
[4] C.C. You, C.L. Huang, C.C. Wei, J.W. Huang, Jpn. J. Appl. Phys. 34 (1995) 1911–1915.
[5] T. Takahashi, Jpn. J. Appl. Phys. 39 (2000) 5637–5641.
[6] I. Molodetsky, P.K. Davies, J. Euro. Ceram. Soc. 21 (2001) 2587–2591.
[7] C.-W. Ahn, S. Nahm, Y.-S. Lim, W. Choi, H.-M. Park, H.-J. Lee, Jpn. J. Appl. Phys. 41 (2002) 5277–5280.
[8] C.-W. Ahn, H.-J. Jang, S. Nahm, H.-M. Park, H.-J. Lee, J. Euro. Ceram. Soc. 23 (2003) 2473–2478.
[9] T.A. Vanderah, Science 298 (2002) 1182–1184.
[10] H. Tamura, T. Konoike, Y. Sakabe, K. Wakino, J. Am. Ceram. Soc. 67 (1984) C59–C61.
[11] P.K. Davies, J. Tong, T. Negas, J. Am. Ceram. Soc. 80 (1997) 1727–1740.
[12] I.M. Reaney, P. Wise, R. Ubic, J. Breeze, N.McN. Alford, D. Iddles, D. Cannell, T. Price, Phil. Mag. A 81 (2001) 501–510.
[13] Archimedes, On Floating Bodies, Vol. I, Proposition 7 (ca 265 BC).
[14] B. Noläng, Inst. Materialkemi, Ångströmlaboratoriet, Box 538, S-751 21 Uppsala, Sweden.
[15] H.M. Rietveld, J. Appl. Crystallogr. 2 (1969) 65.
[16] B.A. Hunter, Rietica-A Visual Rietveld Program, Commission on Powder Diffraction Newsletter 20 (1998) 21.

[17] J. Rodriguez-Carvajal, ILL Internal Report, FULLPROF computer program (1993).
[18] N.E. Brese, M. O'Keeffe, Acta Crystallogr. B 47 (1991) 192–197.
[19] M. Bieringer, S.M. Moussa, L.D. Noailles, A. Burrows, C.J. Kiely, M.J. Rosseinsky, R.M. Ibberson, Chem. Mater. 15 (2003) 586–597.
[20] I. Qazi, I.M. Reaney, W.E. Lee, J. Euro. Ceram. Soc. 21 (2001) 2613–2616.
[21] M.W. Lufaso, Chem. Mater. 16 (2004) 2148–2156.
[22] I.M. Reaney, E.L. Colla, N. Setter, Jpn. J. Appl. Phys. 33 (1994) 3984–3990.